Topological basis for the robust distribution of blood to rodent neocortex

Pablo Blinder[a,1], Andy Y. Shih[a,1], Christopher Rafie[b], and David Kleinfeld[a,c,d,2]

[a]Department of Physics, [b]Division of Biology, [c]Graduate Program in Neurosciences, and [d]Center for Neural Circuits and Behavior, University of California, La Jolla, CA, 92093

Communicated by Harry Suhl, University of California, La Jolla, CA, June 9, 2010 (received for review February 12, 2010)

The maintenance of robust blood flow to the brain is crucial to the health of brain tissue. We examined the pial network of the middle cerebral artery, which distributes blood from the cerebral arteries to the penetrating arterioles that source neocortical microvasculature, to characterize how vascular topology may support such robustness. For both mice and rats, two features dominate the topology. First, interconnected loops span the entire territory sourced by the middle cerebral artery. Although the loops comprise <10% of all branches, they maintain the overall connectivity of the network after multiple breaks. Second, >80% of offshoots from the loops are stubs that end in a single penetrating arteriole, as opposed to trees with multiple penetrating arterioles. We hypothesize that the loops and stubs protect blood flow to the parenchyma from an occlusion in a surface vessel. To test this, we assayed the viability of tissue that was sourced by an individual penetrating arteriole following occlusion of a proximal branch in the surface loop. We observed that neurons remained healthy, even when occlusion led to a reduction in the local blood flow. In contrast, direct blockage of a single penetrating arteriole invariably led to neuronal death and formation of a cyst. Our results show that the surface vasculature functions as a grid for the robust allocation of blood in the event of vascular dysfunction. The combined results of the present and prior studies imply that the pial network reallocates blood in response to changing metabolic needs.

anastomoses | imaging | networks | stroke | vasculature

Highly interconnected networks are a hallmark of many engineered systems, ranging from the power grid to the Internet to Manhattan-like road systems (1–3). The price of additional wiring or roads is apparently offset by the ability to transport power, information, and goods to their destination in the presence of local breaks in the network (4). Furthermore, highly interconnected systems may allow a resource, like power, to be rapidly redistributed from areas with low need to those with high need. Ideally, these two features allow highly interconnected systems to fail gracefully in the presence of high loads, reduced supplies, or damage. Beyond engineered systems, documented examples of highly interconnected transportation networks in mammals are confined to the vasculature of adrenal glands (5), the brain (6), the liver (7), the mesentery (8), and long bones (9).

Within the brain, the pial arteriole network above the cortex has received the most attention (10–13), particularly with regard to studies of experimental stroke (14–20). Yet it is an open challenge to analyze this network in a manner that quantitatively reveals the connection between topology and function (21). Past work provides strong evidence that the flow of blood within the pial network is heavily influenced by the extensive interconnections between branches (i.e., arteriolo-arteriolar anastomoses) (22). First, from the perspective of static resource management, when a single surface vessel suffers a targeted occlusion, blood flow in downstream vessels does not cease but rather is maintained in the surface network through the reversal of flow in the nearest downstream vessel (14). This process implies that the interconnections robustly reroute blood, an effect also seen when a major tributary to the middle cerebral artery (MCA) is occluded (23). Second, the recruitment of collateral flow has been shown to improve cerebral blood flow and clinical outcomes in stroke patients (24, 25). Lastly, the extent of cortical damage after a permanent block of the MCA is reduced in genetically altered animals with augmented anastomoses in their surface vasculature (19). From the perspective of dynamic resource management, focal somatosensory stimulation, either to a single vibrissa (26, 27) or to the forepaw (28), leads to an increase in perfusion at the epicenter of electrical activity in cortex but decreased perfusion in surrounding regions.

Here, we focus on the pial network within the territory of the MCA, which includes all branches of the MCA, from the rhinal vein to the anastomoses with the anterior and posterior cerebral arteries (ACA and PCA, respectively). We ask the following questions: (*i*) What is the spatial extent and degree of connectivity of the pial network? In particular, is there an abstract representation that captures the observed topology? (*ii*) What is the dominant topology of branches that form the penetrating arterioles, which deliver blood from the pial network to the underlying neurons in the parenchyma? (*iii*) Are there qualitative differences between these networks in rats versus mice? (*iv*) Do anastomoses serve to preserve flow to the penetrating arterioles in response to an occlusion to a branch in a surface arteriole?

Results

The primary anatomical data consists of fluorescent vascular fills from four rats, 280 to 320 g in mass, and five mice, 25 to 35 g in mass, in which the cortical mantle was flattened and photographed (Fig. 1*A*). The surface vasculature was traced by hand and codified with the use of graph notation (Fig. 1*B*). An additional 30 rats, 290 to 310 g in mass, served as subjects for measurements of flow and neuronal viability subsequent to focal occlusion of the surface vasculature.

Basic Measures. Without exception, the pial network was found to form a planar graph. Segments of surface vessels correspond to edges (green lines, Fig. 1*A*–*C*), branching points among three edges correspond to vertices with a coordination number of 3 (red dots, Fig. 1*A*–*C*), and points where single penetrating arteriole dive into the parenchyma correspond to vertices with a coordination number of 1 (cyan dots, Fig. 1*A*–*C*). The penetrating arterioles originate *en passant*, as opposed to at the end of the edge of a surface vessel, in $15 \pm 4\%$ (mean $\pm$ SD) of the cases for both rats and mice (Fig. 1*C*). Nearly one-half of the vertices fall into each category, both for rats and mice (Fig. 1*D*). The territory fed by the MCA, defined as the convex hull for the set of branch points delimited by the outer-most penetrating arteries, encompasses ≈ 150 mm^2 for rats and one-third that amount for mice (Table 1). This finding corresponds to about half of the total surface area of the cortical mantle for rat, using

Author contributions: P.B., A.Y.S., and D.K. designed research; P.B., A.Y.S., and C.R. performed research; D.K. contributed new reagents/analytic tools; P.B. and A.Y.S. analyzed data; and P.B., A.Y.S., and D.K. wrote the paper.

The authors declare no conflict of interest.

[1]P.B. and A.Y.S. contributed equally to this work.

[2]To whom correspondence should be addressed. E-mail: dk@physics.ucsd.edu.

This article contains supporting information online at www.pnas.org/lookup/suppl/doi:10.1073/pnas.1007239107/-/DCSupplemental.

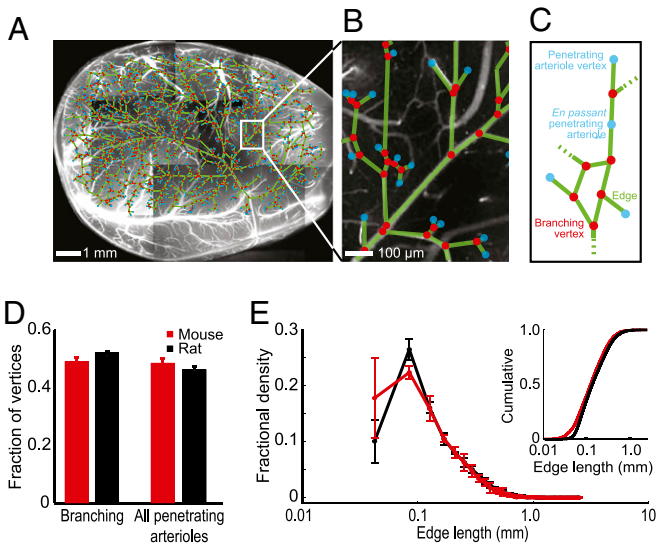

Fig. 1. Complete mapping of the middle cerebral artery. (*A*) A flattened cortical hemisphere from a fluorescent vascular fill, overlaid with a tracing of all vessels within the middle cerebral artery network. (*B*) In each tracing, the edges (green lines) connect vertices positioned at branches, with coordination number of 3 (red circles), and vertices positioned at the location of penetrating arteries (cyan circles). (*C*) Cartoon of the vascular labels that includes penetrating vessels formed *en passant* and at the end of edges. (*D*) The composition of vertices between the rats and mice differ slightly, albeit significantly, in the proportion of branches ($P < 0.05$, t test), but showed no differences in the proportion of vertices at penetrating arterioles. (*E*) The distribution of edge lengths for the entire pial network. There is a small, but significant shift between the distributions for rats and mice ($P < 0.05$, KS test, *Inset*).

300 mm^2 for the surface area of a cortical hemisphere (29), and serves to emphasize the prominence of this vascular network.

We recorded the coordinates of each vertex and calculated the length of all edges. Although the pial network for rats is clearly larger than that for mice (Table 1), the distribution of edge lengths is quite similar between networks for the two species (Fig. 1*E*), with a small, albeit significant ($P < 0.05$, KS–test), difference in the cumulative distribution (*Insert*; Fig. 1*E*). With regard to two additional metrics, the mean length of an edge is similar between the two species—that is, 200 ± 4 μm (mean ± SD) for rats and 175 ± 5 μm (mean ± SD) for mice—and the edges that emanate from a branch point diverge asymmetrically with a mean acute angle near 75° for both species (Fig. S1). In toto, metrics of the vasculature for the two species of rodents are similar.

Interconnected Loops Form a Robust Backbone. We direct our focus to the properties of the MCA backbone. For each network, all vertices with a coordination number of 1 were removed, and all newly formed vertices with coordination numbers of 1 or 2 were iteratively removed, until only the backbone remained (black lines, Fig. 2*A*). In all cases, the backbone spans the full territory of the MCA yet includes only a small fraction of all vertices and edges, and a correspondingly small fraction of the total length (Table 1).

The ratio of vertices to edges is a measure of redundancy of the network. The combined data from rats and mice is consistent with a ratio of 3 to 2 ($r^2 = 0.99, P < 0.001$) (Fig. 2*B*). This edge-to-vertex ratio coincides with that for a simple lattice in which all vertices have a coordination number of 3, such as a hexagonal grid (30); for comparison, the scaling is 1 for binary trees and buses (Fig. 2*B*). The observed edge-to-vertex ratio of 3 to 2 implies that of the 3N/2 edges within backbone with N vertices, N/2 of the edges represent redundant connections, or anastomoses. These anastomoses constitute only 8.4 ± 0.2% (mean ± SE) and 6.2 ± 0.2% of the entire number of edges in the network for rats and mice, respectively.

A second issue is the size of the loops in the pial backbone. For each network, we calculated the set that contained the smallest independent loops, analogous to Kirchhoff loops in circuit theory (Fig. 2*C*). The number of such loops is 3.4 times larger for rats than mice. This finding is not inconsistent with the larger territory of the MCA network in rats versus mice, by a factor of 2.8 (Table 1). The distribution of edges in loops that comprise the backbone has a mode at four edges and is the same for rats and mice (Fig. 2*D*) ($P > 0.1$, KS-test). The predominance of four rather than six edges per loop, together with a coordination number of 3 for each vertex, implies that no obvious lattice captures all features of the pial networks. Lastly, our measures indicate that the probability density of loops with a given area is observed to be exponentially distributed with mean values of 0.94 ± 0.14 mm^2 (mean ± 95% confidence interval) and 0.72 ± 0.06 mm^2 for rat and mice, respectively (Fig. S2).

The robustness of the surface backbone may be quantified by a perturbation procedure that was applied to each of the nine backbone data sets (Fig. 3*A*). We assessed the fraction of vertices within isolated subgraphs (i.e., vertices and edges that are disconnected from the main network) as edges were progressively removed at random. In the limit of a small fraction of deleted edges, the fraction of isolated graphs scales approximately with the size of the network. For the case of networks in rat (n ~ 200 nodes), we find that 12.6% of the backbone edges can be removed before 5% of the vertices are isolated (10^4 simulations per data set) (Fig. 3*A* and *B*). This value compares with 17.4% for a closely-sized hexagonal grid ($n = 294$ nodes) (Fig. 3*B*), which has the same degree vertices but a larger number of edges per loop, and 40.4% for a closely-sized square grid ($n = 225$ nodes) (Fig. 3*B*), which has vertices with a coordination number of 4 but the same average number of edges per loop. To the extent that a hexagonal grid is a valid idealization of the backbone, the resilience of the pial network is within 30% of ideal.

Offshoots from the Backbone End in Penetrating Arterioles. We shift our attention to the offshoots that originate from the pial backbone and give rise to penetrating arterioles, either directly or after branching (Fig. 4*A*). The total number of offshoots per MCA network were 512 ± 88 and 205 ± 37 (mean ± SD), respectively, for the rat and mouse. We labeled the offshoot edges by a modified Strahler hierarchical branching classification (31). Both edges, and *en passant* branches from an edge that lead to penetrating arteries are denoted terminal or order-0 edges in this scheme: the merger of two order-0 edges gives rise to an order-1 edge, and so on. Nearly 75% of offshoots from rats and mice have only order-0 edges: that is, just a single stub as they lead to a penetrating artery (Fig. 4*B*) or are *en*

Table 1. Metrology of rat versus mouse pial vasculature

	Entire pial vasculature		Backbone edges			
	Areal territory (mean ± SD) mm^2	Total length (mean ± SD) mm	Fraction of edges (mean ± SE)	Fraction of vertices (mean ± SE)	Total length (mean ± SD) mm	Number of Kirchhoff loops (mean ± SD)
Rat	145 ± 6	453 ± 12	0.149 ± 0.013	0.106 ± 0.001	260± 26	120.8 ± 7.8
Mouse	52 ± 3	175 ± 9	0.071 ± 0.012	0.062 ± 0.008	76.6 ± 8.5	27.4 ± 2.9

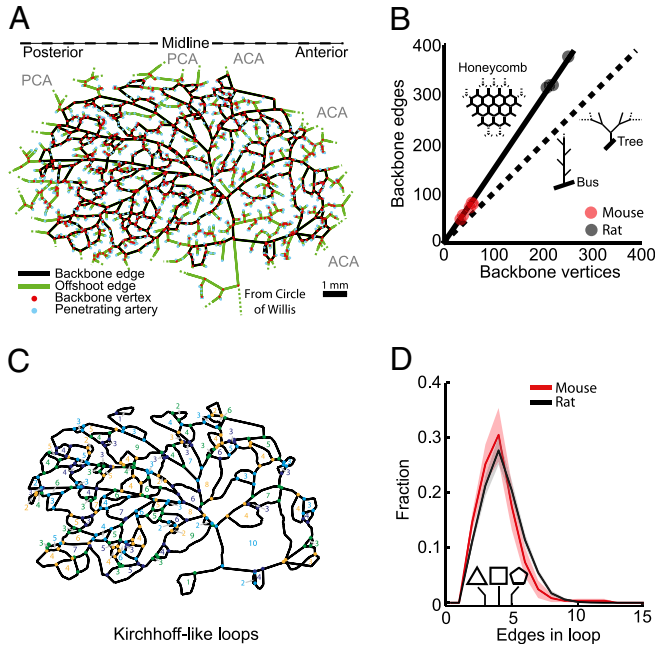

Fig. 2. The backbone loop structure of the pial network. (*A*) Representative example of a complete MCA tracing for rat. The backbone of the MCA is highlighted with black edges and red vertices, nonbackbone offshoots are shown in green. (*B*) The ratio of vertices to edges for the combined data from rats and mice is consistent with a scaling of 3 to 2, equal to that for a hexagonal lattice. For comparison, the scaling is 1 for trees and buses. (*C*) The same backbone as in *A*, but with the set of all loops, chosen to comprise those with the smallest number of edges involved per loop. The number of edges appears in same color as related vertex. (*D*) The distribution of number of edges per loop for rats and mice. Despite the difference in the total number of loops, both species share the same distribution.

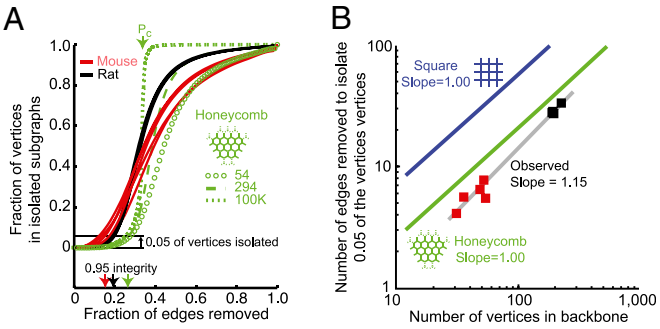

Fig. 3. Structural robustness to cumulative edge removal for measured pial networks and ideal lattices. (*A*) Average backbone robustness to edge removal for networks for rat, mice, and honeycomb lattices of different sizes. Robustness is computed by progressively removing graph edges at random while computing the fractions of vertices that become isolated from the graph's largest component. This process ends with the removal of all edges and it is repeated 10,000 times for each network. The fraction of edges removed that result in isolation of 5% of the vertices are indicated by the color-coded arrows. As a control, the limit in which all vertices approach isolation corresponds to the fraction of vertices that remain disconnected as a path is formed that spans the network. The theoretical value of $2sin(\pi/18) = 0.347$ for percolation in a hexagonal lattice (51) (i.e., the percolation threshold Pc, compares well with the result for simulations with n = 100,000 nodes). (*B*) The number of vertices required to disconnect 5% of the network as a function of the size of the network. Compared with the rodent MCA backbones, an average of 17 and 40% additional edges have to be removed from a honeycomb or a square lattice, respectively, to attain the same extent of isolated vertices.

passant. Offshoots with more than a single order-0 edge occur with a probability that follows an inverse power law (Fig. 4*B*). The structure of these more complex offshoots can be described as trees that never contain more than order-4 edges, buses, or a mixture of these two classes; buses are more common than trees and in mice the largest offshoots have a predominant tree-like structure (Fig. S3). In toto, these findings underscore that the major fraction of penetrating arterioles are sourced directly from an edge of the backbone.

Rerouted Flow in Backbone Loops After a Single-Point Occlusion Acts to Preserve the Underlying Neuronal Viability. Does the observed topology of loops within the MCA backbone (Fig. 3) and a predominance of stubs that source penetrating arterioles (Fig. 4*B*) serve to preserve flow to local penetrating arterioles during occlusions? To test this hypothesis, we used in vivo two-photon laser scanning microscopy (TPLSM) to measure changes in blood flow through penetrating arterioles, in rats, in response to a targeted occlusion to a branch of a surface loop. We first located a surface arteriole loop with several branching penetrating arteriole stubs within the field of a cranial window (Fig. 5*A*). The volume flux of RBCs was measured in a number of proximal penetrating arterioles, including a target vessel fed directly from the loop, as well as neighboring vessels within 200 μm of the target location and one or more penetrating arterioles distant from the target vessel (i.e., greater than 600 μm away). We then formed an intraluminal clot within the lumen of the targeted vessel with localized photothrombosis (14) (Fig. 5*B*). The flux of RBCs was then remeasured in all penetrating vessels that we initially probed.

Our results segregate into two groups based on the initial flux through the penetrating arteriole (Fig. 5*C* and Table S1). An occlusion to a surface arteriole had no impact on the flux through proximally located penetrating arterioles with low initial flux (n = 8), which maintained 1.15 ± 0.12-times (mean ± SE) of their preocclusion levels (cyan points on *Left*, Fig. 5*C*), an insignificant change (P = 0.4, Wilcoxon). The preservation in flux is consistent with maintenance of the velocity of the RBCs as there is no significant compensatory vasodilation (Table S1). In contrast, proximally located penetrating arterioles with high initial flux (n = 10) recovered to only 0.46 ± 0.04-times their preocclusion levels (cyan points on *Right*, Fig. 5*C*), a statistically significant decrease ($P < 0.01$, Wilcoxon). The decrease in flux was caused by an incomplete recovery of the velocity of RBCs ($P < 0.05$, Wilcoxon) and a lack of compensatory vasodilation (Table S1). In nearly all cases, the full or partial maintenance of the flux of RBCs was enabled by reversal of flow in segments of the backbone downstream from the point-occlusion, consistent with a past report of reversals (14). Furthermore, the

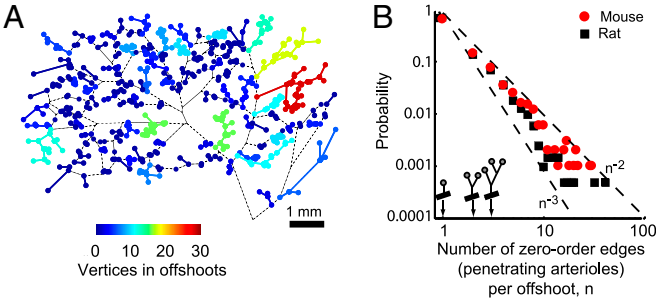

Fig. 4. Penetrating arteries branch from the backbone and directly dive into the parenchyma. (*A*) Example of offshoot branches emerging from a mouse middle cerebral artery backbone. Offshoot branches were isolated into subgraphs that are color coded by the number of vertices per subgraph. (*B*) More than 75% of the offshoots consists of a single penetrating arteriole (n = 2,673 and 1,377 offshoot branches for rat and mouse, respectively). The tail of this distribution is empirically bounded by quadratic and cubic decays.

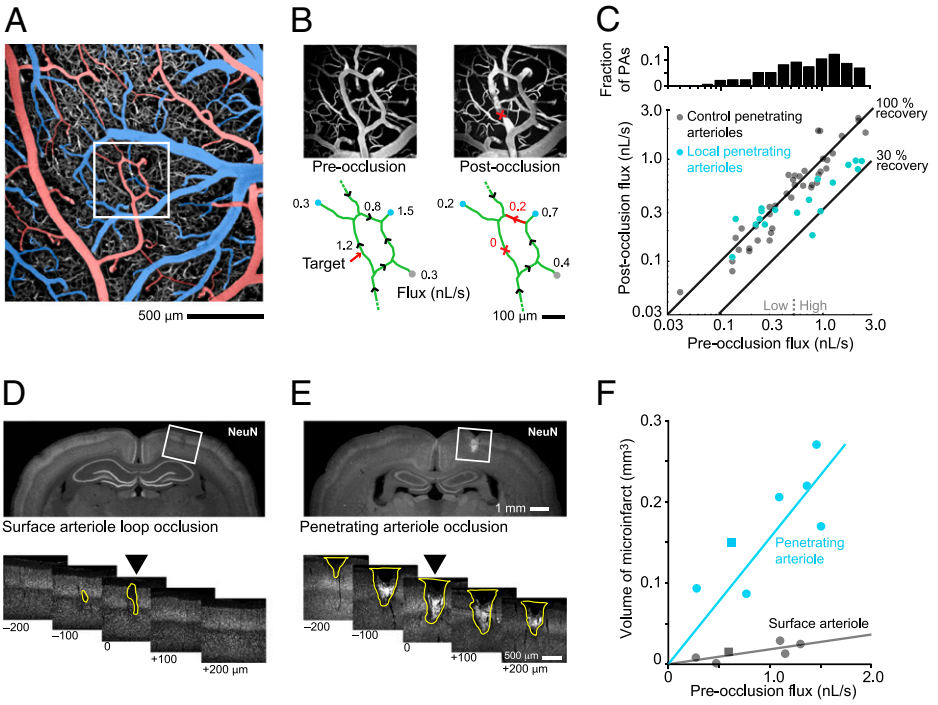

Fig. 5. Preservation of flux through penetrating arterioles after single-point occlusion of a surface arteriole loop. (*A*) Maximal projection of a stack of images collected from the upper 300 μm of rat cortical vasculature using in vivo TPLSM. The pial arteriole network is pseudocolored in red and the venous network in blue. The inset highlights a small arteriole loop with three penetrating arteriole stubs. (*B*) A localized clot is formed in one segment of the surface arteriole loop using targeted photothrombosis (x in loop). Pre- and postocclusion measurements of the flux of RBCs in penetrating arterioles and surface arterioles were collected. Local penetrating arterioles were situated near the targeted surface arteriole, and distant penetrating arterioles were measured as controls. (*C*) Scatter plot of pre- and postocclusion flux through penetrating arterioles. The histogram of the baseline distribution of flux is derived from 399 arterioles. (*D*) Photomicrographs of serial sections, stained with αNeuN, from an animal with a surface occlusion that was killed after 1 week of survival. The box indicates the area photographed at higher magnification; arrow in lower set of photomicrographs. The volume of cortical infarction, highlighted by the dashed line, was determined by measuring loss of αNeuN staining across a contiguous set of serial sections. (*E*) Photomicrographs of serial sections, analyzed as in *D*, from an animal in which a penetrating arteriole was directly occluded by photothrombosis. Note the relatively large infarction. (*F*) Microinfarction volumes plotted as a function of the baseline flux of the target arteriole. The experiments shown in *D* and *E* are marked with square points.

maintained flow in 95% of the vessels exceeded 30% of their initial flux, sufficient to prevent tissue infarction (32–34). As a control, we observed that distant penetrating arterioles were, on average, unaffected by the localized occlusion (n = 40) (gray points, Fig. 5*C*).

We next asked whether the disruption of a surface arteriole loop led to an eventual loss of neuronal viability. We formed a point occlusion to a surface vessel (Fig. 5*B*) and allowed the animals to survive for 1 wk following the occlusion. The health of the underlying tissue was assessed by measuring the volume of dead tissue based on staining with the pan-neuronal marker αNeuN (Fig. 5*D*). We observed very small volumes of infarction in the parenchyma below the occlusion, averaging (n = 6) 0.015 ± 0.004 mm^3 (mean ± SE) (Fig. 5 *D* and *F*), even for volumes with a high initial flux in which the postocclusion flux was significantly reduced (Fig. 5*C*). As a positive control, we compare these findings with damage caused by the complete loss of flow to a single penetrating arteriole. In this case, the photothrombotic clot was formed in the surface branch of a penetrating arteriole before it descends into the parenchyma (35). Occlusions to penetrating arterioles generated infarctions that were an order of magnitude larger in volume than those to a surface vessel, averaging (n = 6) 0.17 ± 0.03 mm^3 (mean ± SE) (Fig. 5 *D* and *F*). In all cases, the volume of the microinfarction was correlated with the baseline flux of the penetrating arteriole (Fig. 5*F*) and the bulk of this variation resulted from an increase in the radial extent of the cyst. Lastly, the average cross-sectional areas of the cyst, 0.16 ± 0.02 mm^2 (mean ± SE), slightly larger than the territory served by each penetrating arteriole as estimated by tessellation of maps (Fig. S4). These findings show that even a partial maintenance of flow in a penetrating arteriole, brought about by rerouting of flow through the pial backbone, is sufficient to preserve long-term neuronal viability subsequent to a surface arteriole occlusion.

Discussion

We analyzed the pial arteriole network that is sourced by the middle cerebral artery in mouse and rat; this network supplies blood to about half of the cortex. Two features of the topology of this network emerge as central to the robust delivery of blood to cortex. The first is that the backbone of the network consists of interconnected loops that span the entire vascular territory (Figs. 1 and 2). The backbone utilizes only 11% of the total arteriole length in the network, as compared with an estimated 7% for a backbone without loops. This implies that the cost of closed loops and the concomitant robust flow is only a 4% increase in the total length of surface vasculature. The loop structure allows the network to remain intact as individual branches are removed; removing 15% of the connections in the backbone isolates only 5% of the cortex from perfusion (Fig. 3). The second feature is that the vast majority of penetrating arterioles that deliver blood from the pial network to the subsurface vasculature originate as stubs that emerge directly from the backbone (Fig. 4). This T-like anatomical arrangement provides two direct pathways for blood to flow to the penetrating arteriole. Consistent with this protective role, a blood clot targeted to an arteriole in the backbone does not disrupt the flow of blood to

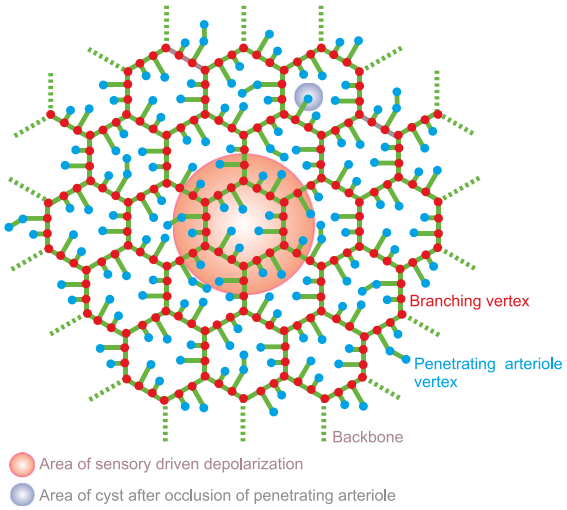

Fig. 6. Idealization of the topology and relative scales of the pial vasculature.

the nearby penetrating arterioles and has relatively little discernable effect on the viability of the underlying tissue (Fig. 5).

The backbone of the pial network may be viewed as a planar graph, with a coordination number of exactly 3 (Fig. 2*B*) and a near-equal proportion of loops with three, four, and five edges (Fig. 2 *C* and *D*). There is no regular lattice that satisfies this constraint. Nonetheless, a honeycomb lattice has the correct coordination number and the same scaling of edges per vertex. Thus, it is the default choice as an idealized albeit imperfect model of the backbone (Figs. 2*B* and 3 *A* and *B*). Lastly, we note that although some past studies describe the pial network of the MCA solely in terms of trees (36, 37), these studies analyzed only relatively small portions of the total network and, furthermore, had low spatial resolution. The present work avoids these limitations and further shows that mice and rats share the same topology (Figs. 1–4 and Table 1). We conjecture, based on comparative studies of pial vasculature (38), that a similar topology is found in higher mammals.

The loop structure facilitates the redistribution of blood during focal activation of a cortical column (28). The area of cortex activated by a punctate stimulus depends on the sensory modality and the state of the animal; for somatotopic cortex in rat, an ~3 mm^2 area is found from measurements of net depolarization of cortex stained with a voltage sensitive dye (27). This value coincides with the area of net vasodilation of surface vessels (28), as well as the area of a net oxygenated hemodynamic signal observed by intrinsic optical imaging (39) (Fig. 6). Consistent with the role of loops in the redistribution of blood from surrounding regions to the center, this area exceeds the estimate of 0.94 mm^2 for the average area of a loop and far exceeds the estimates of 0.13 mm^2 for average area sourced by a penetrating arteriole (35) (Fig. S3) and 0.2 mm^2 for the minimize size of an infarct (17, 20).

A surprising result is that loss of flow to a single penetrating vessel inevitably leads to cortical damage (Fig. 5). This result may have direct clinical relevance. Accumulation of small cortical cysts is involved in pathologies that lead to cognitive decline in humans (40, 41). Recent studies highlight a critical role for small microinfarctions in the cerebral cortex, which are distinct from subcortical lacunae that originate from a blockade in deep penetrating vessels. These microinfarctions are small, ranging between 0.3 and 2 mm in diameter (40), and can be below detection limits of clinical computerized tomography or magnetic resonant imaging. We suggest that cumulative blockage of single penetrating arterioles may be a common element that contributes to cognitive decline. This hypothesis suggests the utility of examining cortical tissue from individuals who exhibited cognitive decline but no overt signatures of stroke.

The occlusion experiments in the present study (Fig. 5) complement past work on the consequences of targeted lesions to pial vessel. In past work, a single occlusion to an arteriole in the backbone leads to a reversal in the direction of flow in one of the two branches that lie immediately downstream from the occlusion (14). The magnitude of the flux in these vessels is, on average, 45% of their initial value and is not considered to be deleterious (32–34). There was no change in the mean flux by two branches downstream. These results demonstrated the resilience of the backbone of the pial network to an occlusion, yet the physiologically relevant issue of preservation of flow to nearby penetrating arterioles was not addressed. In the present work, we show that flow through the pial backbone compensates for an occlusion that is even proximal to a penetrating arteriole (Fig. 5 *B* and *C*). This compensation is complete for penetrating arterioles with a small initial flux and at the 45% level for those with large initial flux, again within the range of physiologically acceptable flow (32–34) (Fig. 5*C*). Long-term changes in the vasculature could compensate for this hypoperfusion and ameliorate potential damage at threshold levels of flow (42, 43).

The development of cysts subsequent to blockage of a single penetrating arteriole (Fig. 5*F*) yields insight into the extensive damage that is expected to occur when penetration arterioles originate from trees, or buses, off the backbone rather than as lone offshoots (Fig. 4). A clot anywhere within the tree would lead to a loss of flow to all downstream penetrating arterioles. The tissue damage caused by such an occlusion is expected to be proportional to the number of penetrating arterioles fed by the tree, because the volume of a cyst is positively correlated with the initial flux of the occluded penetrating arteriole (Fig. 5*F*). Fortunately, penetrating arterioles that originate from trees and buses represent a minor proportion of branches from the pial backbone (Fig. 4*A*). This fraction was conservatively estimated at 20–25% (Fig. 4*B*); this includes a systematic overestimate as branches at the border of the MCA territory may be part of loops that involve the ACA and PCA (Fig. 2*A*).

Fault tolerance of blood flow to cortex is organized in three tiers. The highest level is global and consists of the routing of blood in the circle of Willis (6), so that all of the cerebral arteries are sourced even if one of the common carotid arteries is blocked or impaired. The middle level comprises the anastomoses between the perimeter of the region primarily sourced by the MCA and those sourced by the ACA and PCA (Fig. 2*A*). Both naturally occurring (23, 44) and genetically induced (19) changes in the nature of these anastomoses lead to a detrimental ischemic outcome following occlusion of the MCA. At the lowest level, described in this article, redundancy is attained by means of loops formed by pial anastomoses between the branches of the MCA. These loops provides for the rerouting of blood to preserve flow in the face of both local obstructions (14) (Fig. 5) and a global decrease in perfusion (14, 45).

Methods

We generated angiograms of the MCA by transcardial perfusion of mice and rats with a gel perfusate cross-linked with fluorescein, as described (46). The perfused brain was removed from the skull under extreme care to avoid disruption of the pial network, and the two cortices were dissected along the ventricles and flattened between two coverslips separated by a spacer, 3.6 mm for rats and 1.8 mm for mice (Fig. 1*A*). Following flattening, one of the hemispheres was imaged using a MVX10 Macroview fluorescent microscope (Olympus) with a 0.63×, 0.15 NA objective. A set of 9 to 12 overlapping images spanned the hemisphere; the individual images were manually stitched into a single composite for the manual tracing of all branches. Fine processes and ambiguities were resolved by reevaluation of the tissue with an AxioPlan 2 microscope (Zeiss) with a 20×, 0.75 NA objective. This step was particularly critical near the proximal end of the MCA (Fig. S5), where there are relatively few penetrating arterioles (Fig. 2*A* and Fig. S4).

Measurements of the flux of RBCs through pial surface arterioles and penetrating arterioles made use of in vivo TPLSM (47), and anesthetized ani-

mals in which the blood plasma was labeled with fluorescein conjugated dextran (2 MDa), as described (48), and physiological parameters were measured throughout the experiment (Table S2). To accurately quantify changes in the flux of blood flow brought about by the occlusion, we used an arbitrary scan path for the laser beam to simultaneously assess the velocity of RBCs in individual arterioles as well as the diameter of the lumen of the vessel (49). The flux of RBCs, typically averaged over 100 s of data, was calculated from these measurements.

Occlusions were targeted to single pial and penetrating vessels, as described (14, 35, 50). Animals were allowed to recover and were killed for histological analysis 6 to 8 d after the occlusion. We stained with antibodies for NeuN, as described (46), and outlined the regions of tissue with labeled neurons (45) and calculated their 3D area from successive sections (Fig. 5 *E* and *F*).

The care and experimental manipulation of our mice and rats have been reviewed and approved by the Institutional Animal Care and Use Committee at the University of California at San Diego.

ACKNOWLEDGMENTS. We thank Miki Kelly for assistance with obtaining the angiograms, Beth Friedman for instruction on histology, Eshel Ben-Jacob, Robert Desimone, Adrienne L. Fairhall, Marcelo Magnasco, Partha P. Mitra, and Phillip Pincus for discussions on analysis and interpretation, and Jonathan D. Driscoll for comments on an early version of the manuscript. D.K. would like to acknowledge Thomas A. Woolsey for early advice in the study of cortical blood flow. This work was supported by National Institutes of Health Grants EB003832, MH085499, and NS059832 (to D.K.), a Bikura fellowship from the Israeli Science Foundation (to P.B.), and a fellowship from the American Heart Association (to A.Y.S.).

1. Schewe PF (2007) *The Grid: A Journey Through the Heart of Our Electrified World* (Joseph Henry Press, Washington, DC).
2. Albert R, Barabasi A-L (2002) Statistical mechanics of complex networks. *Rev Mod Phys* 74:47–97.
3. Banavar JR, Maritan A, Rinaldo A (1999) Size and form in efficient transportation networks. *Nature* 399:130–132.
4. Bohn S, Magnasco MO (2007) Structure, scaling, and phase transition in the optimal transport network. *Phys Rev Lett* 98:088702.
5. Thongpila S, et al. (1998) Adrenal microvascularization in the common tree shrew (*Tupaia glis*) as revealed by scanning electron microscopy of vascular corrosion casts. *Acta Anat (Basel)* 163:31–38.
6. Scremin OU (1995) Cerebral vascular system. *The Rat Nervous System*, ed Paxinos G (Academic Press, Inc., San Diego), 2nd Ed.
7. Haratake J, Yamamoto O, Hisaoka M, Horie A (1990) Scanning electron microscopic examinations of microvascular casts of the rat liver and bile duct. *J UOEH* 12: 19–28.
8. Pries AR, Secomb TW, Gaehtgens P (1996) Relationship between structural and hemodynamic heterogeneity in microvascular networks. *Am J Physiol* 270:H545–H553.
9. Trias A, Fery A (1979) Cortical circulation of long bones. *J Bone Joint Surg Am* 61: 1052–1059.
10. Fox G, Gallacher D, Shevde S, Loftus J, Swayne G (1993) Anatomic variation of the middle cerebral artery in the Sprague-Dawley rat. *Stroke* 24:2087–2092, discussion 2092–2093.
11. Brozici M, van der Zwan A, Hillen B (2003) Anatomy and functionality of leptomeningeal anastomoses: A review. *Stroke* 34:2750–2762.
12. Niiro M, Simon RP, Kadota K, Asakura T (1996) Proximal branching patterns of middle cerebral artery (MCA) in rats and their influence on the infarct size produced by MCA occlusion. *J Neurosci Methods* 64:19–23.
13. Bär T (1980) The vascular system of the cerebral cortex. *Adv Anat Embryol Cell Biol* 59: I–VI, 1–62.
14. Schaffer CB, et al. (2006) Two-photon imaging of cortical surface microvessels reveals a robust redistribution in blood flow after vascular occlusion. *PLoS Biol* 4:e22.
15. Longa EZ, Weinstein PR, Carlson S, Cummins R (1989) Reversible middle cerebral artery occlusion without craniectomy in rats. *Stroke* 20:84–91.
16. Wei L, Rovainen CM, Woolsey TA (1995) Ministrokes in rat barrel cortex. *Stroke* 26: 1459–1462.
17. Zhang S, Murphy TH (2007) Imaging the impact of cortical microcirculation on synaptic structure and sensory-evoked hemodynamic responses in vivo. *PLoS Biol* 5: e119.
18. Pinard E, Engrand N, Seylaz J (2000) Dynamic cerebral microcirculatory changes in transient forebrain ischemia in rats: Involvement of type I nitric oxide synthase. *J Cereb Blood Flow Metab* 20:1648–1658.
19. Maeda K, Hata R, Bader M, Walther T, Hossmann KA (1999) Larger anastomoses in angiotensinogen-knockout mice attenuate early metabolic disturbances after middle cerebral artery occlusion. *J Cereb Blood Flow Metab* 19:1092–1098.
20. Sigler A, Mohajerani MH, Murphy TH (2009) Imaging rapid redistribution of sensory-evoked depolarization through existing cortical pathways after targeted stroke in mice. *Proc Natl Acad Sci USA* 106:11759–11764.
21. Hudetz AG (1993) Percolation phenomenon: The effect of capillary network rarefaction. *Microvasc Res* 45:1–10.
22. Mchedlishvili G (1963) *Arterial Behavior and Blood Circulation in the Brain* (Consultants Bureau, NY).
23. Rubino GJ, Young W (1988) Ischemic cortical lesions after permanent occlusion of individual middle cerebral artery branches in rats. *Stroke* 19:870–877.
24. Liebeskind DS (2003) Collateral circulation. *Stroke* 34:2279–2284.
25. Maas MB, et al. (2009) Collateral vessels on CT angiography predict outcome in acute ischemic stroke. *Stroke* 40:3001–3005.
26. Cox SB, Woolsey TA, Rovainen CM (1993) Localized dynamic changes in cortical blood flow with whisker stimulation corresponds to matched vascular and neuronal architecture of rat barrels. *J Cereb Blood Flow Metab* 13:899–913.
27. Derdikman D, Hildesheim R, Ahissar E, Arieli A, Grinvald A (2003) Imaging spatiotemporal dynamics of surround inhibition in the barrels somatosensory cortex. *J Neurosci* 23: 3100–3105.
28. Devor A, et al. (2007) Suppressed neuronal activity and concurrent arteriolar vasoconstriction may explain negative blood oxygenation level-dependent signal. *J Neurosci* 27:4452–4459.
29. Nieuwenhuys R, Ten Donkelaar HJ, Nicholson C (1998) *The Central Nervous System of Vertebrates* (Springer, Berlin), Vol 3.
30. Stokman FN (1980) Graph theoretical elaboration of cumulative scaling techniques. *Qual Quant* 14:277–288.
31. Strahler AN (1952) Dynamic basis of geomorphology. *Geol Soc Am Bull* 63:923–938.
32. Baron JC (2001) Perfusion thresholds in human cerebral ischemia: Historical perspective and therapeutic implications. *Cerebrovasc Dis* 11(Suppl 1):2–8.
33. Zhao W, Belayev L, Ginsberg MD (1997) Transient middle cerebral artery occlusion by intraluminal suture: II. Neurological deficits, and pixel-based correlation of histopathology with local blood flow and glucose utilization. *J Cereb Blood Flow Metab* 17: 1281–1290.
34. Hossmann KA (1994) Viability thresholds and the penumbra of focal ischemia. *Ann Neurol* 36:557–565.
35. Nishimura N, Schaffer CB, Friedman B, Lyden PD, Kleinfeld D (2007) Penetrating arterioles are a bottleneck in the perfusion of neocortex. *Proc Natl Acad Sci USA* 104: 365–370.
36. Lapi D, Marchiafava PL, Colantuoni A (2008) Geometric characteristics of arterial network of rat pial microcirculation. *J Vasc Res* 45:69–77.
37. Hermán P, Kocsis L, Eke A (2001) Fractal branching pattern in the pial vasculature in the cat. *J Cereb Blood Flow Metab* 21:741–753.
38. Mchedlishvili G, Kuridze N (1984) The modular organization of the pial arterial system in phylogeny. *J Cereb Blood Flow Metab* 4:391–396.
39. Simons SB, Chiu J, Favorov OV, Whitsel BL, Tommerdahl M (2007) Duration-dependent response of SI to vibrotactile stimulation in squirrel monkey. *J Neurophysiol* 97:2121–2129.
40. Suter OC, et al. (2002) Cerebral hypoperfusion generates cortical watershed microinfarcts in Alzheimer disease. *Stroke* 33:1986–1992.
41. Kövari E, et al. (2007) Cortical microinfarcts and demyelination affect cognition in cases at high risk for dementia. *Neurology* 68:927–931.
42. Coyle P (1984) Diameter and length changes in cerebral collaterals after middle cerebral artery occlusion in the young rat. *Anat Rec* 210:357–364.
43. Zhang H, Prabhakar P, Sealock R, Faber JE (2010) Wide genetic variation in the native pial collateral circulation is a major determinant of variation in severity of stroke. *J Cereb Blood Flow Metab* 30:923–934.
44. Coyle P, Feng X (1993) Risk area and infarct area relations in the hypertensive stroke-prone rat. *Stroke* 24:705–709, discussion 710.
45. Shih AY, et al. (2009) Active dilation of penetrating arterioles restores red blood cell flux to penumbral neocortex after focal stroke. *J Cereb Blood Flow Metab* 29:738–751.
46. Tsai PS, et al. (2009) Correlations of neuronal and microvascular densities in murine cortex revealed by direct counting and colocalization of nuclei and vessels. *J Neurosci* 18:14553–14570.
47. Svoboda K, Denk W, Kleinfeld D, Tank DW (1997) In vivo dendritic calcium dynamics in neocortical pyramidal neurons. *Nature* 385:161–165.
48. Kleinfeld D, Mitra PP, Helmchen F, Denk W (1998) Fluctuations and stimulus-induced changes in blood flow observed in individual capillaries in layers 2 through 4 of rat neocortex. *Proc Natl Acad Sci USA* 95:15741–15746.
49. Driscoll JD, Shih AY, Drew PJ, Kleinfeld D (2010) Quantitative two-photon imaging of blood flow in cortex. *Imaging in Neuroscience and Development*, ed Yuste R (CSHL Press, NY), Vol 2.
50. Shih AY, et al. (2009) Optical-based models of single vessel occlusion in rodent neocortex. *Imaging in Neuroscience and Development*, ed Yuste R (CSHL Press, NY), Vol 2.
51. Larson RG, Scriven LE, Davis HT (1981) Percolation theory of two phase flow in porous media. *Chem Eng Sci* 36:57–73.